

Optimizing the pump coupling for a three-wave mixing Josephson parametric amplifier

Wei Dai,^{1,*} Gangqiang Liu,¹ Vidul Joshi,¹ Alessandro Miano,¹
Volodymyr Sivak,¹ Shyam Shankar,^{1,2} and Michel H. Devoret^{1,†}

¹*Department of Applied Physics, Yale University, New Haven, CT 06520, USA*

²*Chandra Department of Electrical and Computer Engineering,
University of Texas at Austin, Austin, TX 78712, USA*

(Dated: November 12, 2024)

Josephson element-based parametric amplifiers (JPAs) typically require rf pump power that is several orders of magnitude stronger than the maximum signal power they can handle. The low power efficiency and strong pump leakage towards signal circuitry could be critical concerns in application. In this work, we discuss how to optimize the pump coupling scheme for a three-wave mixing JPA by employing microwave filtering techniques, with the goal of maximizing the pump power efficiency and minimize pump leakage without sacrificing other properties of interest. We implement the corresponding filter design in a SNAIL-based JPA and demonstrate more than three orders of magnitude improvement in both power efficiency and pump leakage suppression compared to a similar device with regular capacitive coupling, while maintaining state-of-the-art dynamic range and near-quantum-limited noise performance. Furthermore, we show experimentally that the filter-coupled JPA is more robust against noise input from the pump port, exhibiting no significant change in added noise performance with up to 4 K of effective noise temperature at the pump port.

I. INTRODUCTION

Josephson element-based parametric amplifiers (JPAs)[1] have become critical tools in quantum measurements in which the information is carried by a few microwave photons. These amplifiers provide large gain with near quantum-limited added noise, enabling highly efficient microwave measurements in single-shot qubit readout[2], electron spin resonance detection[3], and axion search[4]. Recent research has focused on improving JPA bandwidth and compression power[5–12], which is necessary for multiplexed qubit readout[13, 14] in large-scale quantum processors. However, a major challenge in operating a large array of JPAs at millikelvin temperature is the heat load added to the cryostat by the microwave drives applied for amplification, commonly referred to as the ‘pump’.

To achieve quantum-limited noise performance with a JPA, the pump is typically delivered to the JPA through a heavily attenuated transmission line to reduce thermal noise. In addition, the pump line is weakly coupled to the JPA, usually with a small capacitance or mutual inductance, to minimize the signal photon loss. As a result of these choices, the pump power required by the JPA is usually several orders of magnitude higher than the signal power. For instance, a state-of-the-art 3-wave-mixing JPA dissipates around 0.01 to 1 μW of power on the base plate of a dilution refrigerator, whose cooling power is typically 10 to 100 μW at 20 mK [15]. This is a practical limiting factor in scaling up superconducting quantum processors.

In addition, the strong pump power incident on the JPA also poses challenges for protecting qubits against

unwanted back-action. Since the coupling strength on the signal port is much higher than that on the pump port, the intra-amplifier pump photons predominantly exit the amplifier through the signal port and propagate towards the signal source. It usually requires multiple non-reciprocal components (other than the circulator shown in Fig. 1) or filters to achieve sufficient isolation of the pump leakage from the signal source. These elements reduce readout efficiency due to their insertion loss, and can emit thermal photons that dephase the qubit due to heating by the pump leakage.

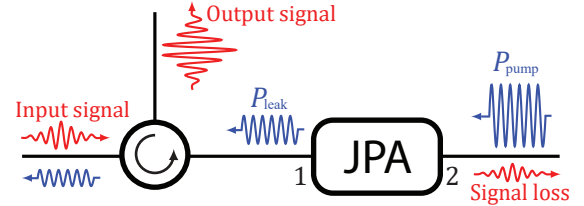


FIG. 1: Minimal schematic describing a reflection JPA as the first stage of the amplifier chain, illustrating the problems addressed in this article. Red arrows indicate information-carrying signal and blue arrows indicate pump. There is generally a trade-off between signal loss and the required pump power at port 2. Furthermore, one circulator at port 1 (for signal directionality) is not sufficient to isolate pump leakage from the input circuitry.

Therefore, reducing the pump power needed to operate JPAs is crucial for deploying large-scale systems and for improving the readout performance and qubit coherence. In addition, broadband and higher compression power JPAs for multiplexed qubit readout often demands elevated intra-amplifier pump power [10, 12, 15–17]. Hence, it is desirable to increase pump power coupling at the

* wei.dai.wd279@yale.edu

† michel.devoret@yale.edu

pump port while further suppressing pump leakage from the signal port.

JPAs with pump tones far detuned from the signal frequency offer the opportunity to address these issues by applying microwave filtering techniques. In this work, we demonstrate near 30 dB reduction in both pump power and pump leakage in a three-wave mixing SNAIL parametric amplifier (SPA) by upgrading its capacitively coupled ports with on-chip filters, while retaining its near quantum-limited noise performance. These improvements would enable deployment of a large bank of parallel SPAs with minimal heat load added to the cryostat, facilitating scaling up of superconducting quantum processors. The technique introduced in this work is also applicable to 4-wave-mixing parametric amplifiers with sideband pumping[18], and more generally to other parametric processes activated by off-resonant pumps.

This article is organized as followed: in Section II we introduce *power efficiency* as the metric for characterizing the efficiency of converting pump power to output signal power of a JPA and formulate its optimization as a specific circuit synthesis problem. In Section III we demonstrate a realization of a filter-coupled SPA that fulfills the optimization goals. In Section IV we compare the filter-coupled SPA with a standard capacitor-coupled SPA and demonstrate improvements in both power efficiency and pump leakage suppression. In Section V, we show the improved noise rejection at signal frequency on the pump port of the filter-coupled SPA, which would allow the amplifier to achieve near quantum-limited noise performance with reduced attenuation on the pump line and further decreases its head load to the cryostat.

II. OPTIMIZATION OF JPA POWER EFFICIENCY

A parametric amplifier converts power from its pump into the output signal. The figure-of-merit that characterizes the efficiency of this process is the *power efficiency*, η_p defined as the ratio between the output signal power at 1-dB gain compression point ($P_{1\text{dB}}^{\text{out}}$), and the corresponding pump power (P_{pump}):

$$\eta_p = \frac{P_{1\text{dB}}^{\text{out}}}{P_{\text{pump}}} \quad (1)$$

JPAs typically have power efficiency ranging from 10^{-2} to 10^{-6} , as reviewed in [15]. The power efficiency of 3-wave-mixing JPAs [7, 8, 17, 19–22], due to the large frequency detuning of the pump, is generally orders of magnitude lower than that of their 4-wave-mixing counterparts [5, 10, 22]. In this section, we formulate the goals and constraints for optimizing JPA power efficiency within the framework of network synthesis.

We limit our discussion to the current-pumped JPA whose nonlinearity originates from a *lumped* Josephson element. In

particular, we consider a 3-wave-mixing JPA operating in the phase-preserving mode, in which the wave components at pump frequency ω_p , signal frequency ω_s , and idler frequency $\omega_i = \omega_p - \omega_s$ are coupled via the 3rd-order nonlinearity of the Josephson dipole.

As illustrated in Fig. 2(a), we view the linear embedding circuit of the Josephson dipole in the JPA as a microwave network with two external ports connected to the signal and pump sources respectively, and one internal port loaded by the Josephson dipole. We perform signal-flow analysis on the system at pump and signal frequencies separately, in order to formulate the power efficiency and amplification performance in terms of the circuit parameters.

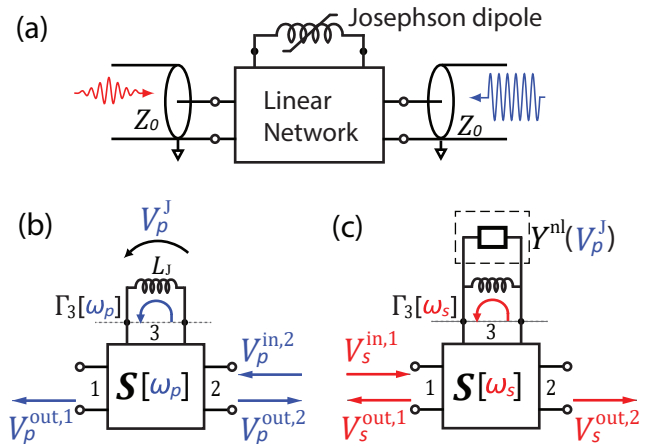


FIG. 2: Modeling the JPA as a scattering system. (a) The JPA consists of a lumped Josephson dipole embedded in a linear network, which has two external ports and one internal port. The external ports - port 1 and port 2 - connect to the signal and pump source respectively. The internal port - port 3 - is loaded by the Josephson dipole. (b) The pump at frequency ω_p is applied from port 2, creating a voltage phasor V_p^J at the Josephson dipole. (c) At signal frequency ω_s , the Josephson dipole produces an additive admittance arising from pumping. Reflection gain for the signal is measured from port 1.

To relate the power efficiency to the circuit parameters in Fig. 2(b), we first rewrite the definition (1) as

$$\eta_p = \frac{P_{1\text{dB}}^{\text{out}}}{P_p^J} \cdot \frac{P_p^J}{P_{\text{pump}}} \quad (2)$$

where $P_p^J = |V_p^J|^2 / \omega_p L_J$ is the steady-state pump power on the Josephson dipole created by the pump tone applied on port 2. The first factor in Eq. (2) is the ratio between the output signal power at 1 dB gain compression point and the pump power incident onto the Josephson dipole. We will refer to this factor as the *nonlinear mixing efficiency* η_p^{nl} . The second factor in Eq. (2) is the ratio between the pump power incident onto the Josephson dipole and the power $P_{\text{pump}} = |V_p^{\text{in},2}|^2 / Z_0$ incident

on the device pump port, which we will refer to as the *pump coupling efficiency* η_p^c . Hence $\eta_p = \eta_p^{\text{nl}}\eta_p^c$.

The power efficiency of a JPA can be improved by increasing the nonlinear mixing efficiency η_p^{nl} and/or the pump coupling efficiency η_p^c . Improving η_p by increasing η_p^{nl} has been demonstrated in experiment. For example, by operating a 3-wave-mixing JPA at its ‘Kerr-free’ point, where the 4th-order nonlinearity is minimized, the $P_{\text{1dB}}^{\text{out}}$ can be improved by more than 10 dB under similar pump power [15]. Recently, a general method for engineering higher-order nonlinearities of Josephson elements for better JPA power efficiency has been proposed [23]. However, it is important to note that getting η_p^{nl} close to unity leads to the effect of pump depletion[1, 24], causing the device to deviate from the linear amplifier regime. More investigation is required for a JPA operated in the pump depletion regime.

In this work, we instead focus on improving η_p by maximizing η_p^c , which amounts to establishing the desired P_p^J across the Josephson dipole with minimal pump power P_{pump} . In contrast to η_p^{nl} , engineering η_p^c to its theoretical upper limit of unity does not lead to pump depletion.

Furthermore, increasing η_p^c also helps suppress the pump leakage from the signal port (port 1). Assuming no loss in the circuit, conservation of the pump power requires:

$$\frac{|V_p^{\text{out},1}|^2}{Z_0} + \frac{|V_p^{\text{out},2}|^2}{Z_0} = \frac{|V_p^{\text{in},2}|^2}{Z_0} = \frac{P_p^J}{\eta_p^c} \quad (3)$$

in which $P_{\text{leak}} = |V_p^{\text{out},1}|^2/Z_0$ is the pump leakage power. Therefore, the pump leakage power scales as and is upper bounded by P_p^J/η_p^c , and improving η_p^c will generally reduce pump leakage. We will discuss further suppression of pump leakage in Section III and Section IV by filtering on the signal port.

The pump coupling efficiency of the JPA is obtained by analyzing the circuit in Fig. 2(b), where we approximate the nonlinear Josephson dipole as a linear inductance L_J . The voltage across the Josephson dipole created by the pump, V_p^J , can be evaluated with respect to the input phasor $V_p^{\text{in},2}$. The pump coupling efficiency is thus given by:

$$\eta_p^c = \left| \frac{1 + \Gamma_3[\omega_p]}{1 - \Gamma_3[\omega_p]S_{33}[\omega_p]} S_{32}[\omega_p] \right|^2 \frac{Z_0}{\omega_p L_J} \quad (4)$$

where $\Gamma_3[\omega_p] = \frac{j\omega_p L_J - Z_0}{j\omega_p L_J + Z_0}$ is the reflection coefficient from the linear inductance L_J loading port 3 of the network, $S_{33}[\omega_p]$ and $S_{32}[\omega_p]$ are the scattering parameters of the network. Therefore, maximizing the pump coupling efficiency amounts to a linear network synthesis problem.

We now discuss the requirements for the circuit to operate as a resonant amplifier. First, a standing wave eigenmode must exist in the circuit. This requirement is captured by the following *Laplace domain* equation:

$$Z^{\text{Th}}(s) + sL_J = 0 \quad (5)$$

where $Z^{\text{Th}} = Z_0(1 + S_{33})/(1 - S_{33})$ is the Thevenin impedance viewed by the Josephson dipole. The solution of Eq. (5), $s_0 = j\omega_0 - \frac{\kappa_0}{2}$, provides the resonance frequency ω_0 and external coupling rate κ_0 for the electromagnetic eigenmode of the system. Eq. (5) and its reformulation in the Fourier domain are discussed in Appendix C.

Second, signal power gain is expected in reflection from port 1, which is given by:

$$G = \left| \frac{V_s^{\text{out},1}}{V_s^{\text{in},1}} \right|^2 = \left| S_{11}[\omega_s] + \frac{S_{13}[\omega_s]\Gamma_3[\omega_s]S_{31}[\omega_s]}{1 - \Gamma_3[\omega_s]S_{33}[\omega_s]} \right|^2 \quad (6)$$

where $\Gamma_3[\omega_s]$ is the reflection coefficient loading port 3 at the signal frequency controlled by the pump. Under the *stiff pump approximation*[1], $\Gamma_3[\omega_s]$ from a current-pumped Josephson dipole is obtained from a linearized model similar to the flux-pumped case [25–27] (see Appendix D for details). In our model, as illustrated in Fig. 2(c), the response of the Josephson dipole at signal frequency is represented by the inductance L_J in parallel with an effective admittance $Y^{\text{nl}}(V_p^J)$ arising from pumping. This gives rise to the reflection coefficient:

$$\Gamma_3[\omega_s] = \frac{1 - Z_0 \left(\frac{1}{j\omega_s L_J} + Y^{\text{nl}}(V_p^J) \right)}{1 + Z_0 \left(\frac{1}{j\omega_s L_J} + Y^{\text{nl}}(V_p^J) \right)} \quad (7)$$

Amplification for the signal requires $|\Gamma_3[\omega_s]| > 1$, which translates into $Y^{\text{nl}}(V_p^J)$ having a negative real part. Moreover, achieving high gain ($G \gg 1$) requires $1 - \Gamma_3[\omega_s]S_{33}[\omega_s] \approx 0$, which is satisfied for near-resonance signals ($\omega_s \approx \omega_0$), as explained in Appendix D.

Lastly, to achieve a noise performance approaching the quantum limit, it requires minimizing the signal loss via port 2. The transmission coefficient from port 1 to port 2 at signal frequency is given by:

$$T = \left| \frac{V_s^{\text{out},2}}{V_s^{\text{in},1}} \right|^2 = \left| S_{21}[\omega_s] + \frac{S_{23}[\omega_s]\Gamma_3[\omega_s]S_{31}[\omega_s]}{1 - \Gamma_3[\omega_s]S_{33}[\omega_s]} \right|^2 \quad (8)$$

Near-quantum-limited noise performance for reflection gain requires $T \ll G$, essentially demanding $|S_{23}[\omega_s]| \ll |S_{13}[\omega_s]|$. In the standard design with capacitively coupled ports, for example, this condition is satisfied by having a large coupling capacitance at port 1 and a small coupling capacitance at port 2. This choice, however, leads to poor transmission at pump frequency from port 2 as well, conflicting with the demand for large pump coupling efficiency given in Eq. (4).

The frequency separation between the pump and signal for the 3-wave-mixing process provides an opportunity to satisfy these seemingly conflicting requirements. In the following sections, we demonstrate that the optimization goals at pump frequency ω_p and signal frequency ω_s can be achieved simultaneously by engineering the coupling network to be strongly frequency selective on a 3-wave-mixing JPA.

III. REALIZATION OF A FILTER-COUPLED SNAIL PARAMETRIC AMPLIFIER

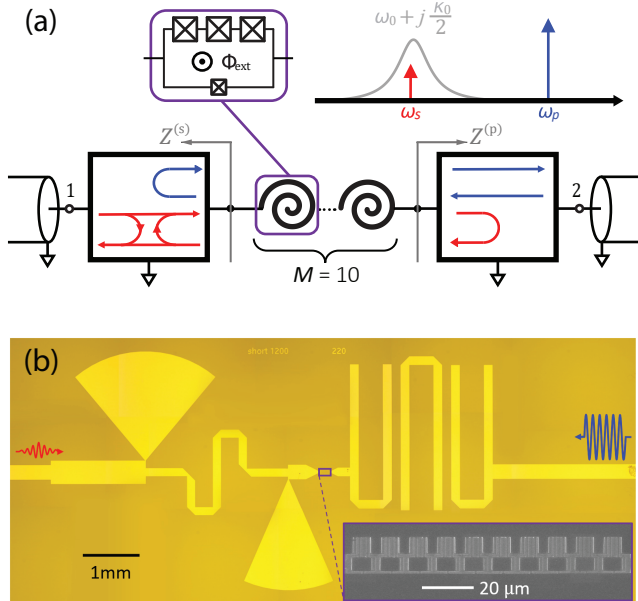


FIG. 3: Filter-coupled JPA in which the Josephson dipole is a SNAIL array. (a) Schematic of a SNAIL parametric amplifier with two filters as coupling networks, with the signal flow graphs representing the desired scattering properties at signal (red) and pump (blue) frequencies respectively. The frequency landscape is sketched in the top right. (b) Optical image of a microstrip device designed to achieve the indicated scattering properties, with an SEM image of the array of 10 SNAILs.

In the last section, the goals and requirements for the circuit synthesis are formulated in terms of the scattering parameters of a 3-port linear network. However, it is technically challenging to directly synthesize this 3-port network in distributed-element circuit. Therefore, as illustrated in Fig. 3(a), we separate the design into two 2-port networks – a pump-port network and a signal-port network, with an array of SNAILs[28] embedded in between, playing the role of the Josephson dipole. The pump-port network prevents transmission at signal frequency ω_s while providing near unity transmission at pump frequency ω_p . Conversely, the signal-port network prevents transmission at ω_p while allowing partial transmission at ω_s with a rate κ_0 , which is critical in forming the resonant mode of the amplifier. The signal-port network also suppresses pump leakage in addition to the suppression originating from the improved pump coupling efficiency according to Eq. (3).

Instead of the standard two-port microwave filter synthesis process based on scattering parameters[29, 30], we formulated the design goals using the output impedances

$Z^{(s)}$ and $Z^{(p)}$, viewed from each end of the Josephson dipole towards the signal and pump ports as shown in Fig. 3(a), respectively. This allows the resonance condition for the concatenated circuit to be represented as an additional constraint on the sum of the two impedances $Z^{(s)} + Z^{(p)} = Z^{\text{Th}}$ according to Eq. (5). We discuss in Appendix B how to bridge between the output impedances and the scattering parameters, and how to formulate the resonance condition.

For compatibility with our in-house fabrication and packaging process (Appendix A), we designed and implemented the amplifier in a microstrip architecture. We employed a compact 3-stage hairpin bandpass filter (with the poles near ω_p) for the pump-port network and a 3-stage radial-stub lowpass filter for the signal-port network to achieve the desired frequency-selective properties. Specifically, the slow frequency roll-off property of the radial-stub lowpass filter allows us to position the amplifier mode within its transition band, facilitating control of κ_0 .

The synthesis process is conducted using AWR Microwave Office. We began by parameterizing the dimensions of the hairpin and radial-stub filter structures in the distributed element circuit. Initial design parameters were chosen to achieve desired filtering performance within the intended signal frequency band (4.8-5.2 GHz) and pump frequency band (9.6-10.4 GHz). In addition, we aimed for a resonant mode with the following properties: (1) resonance frequency $\omega_0/2\pi \approx 5$ GHz, (2) linewidth $\kappa_0/2\pi \approx 100$ MHz (dominated by external coupling via the signal port), (3) external coupling rate via the pump port below 0.5 MHz. These requirements were formulated into constraints on the output impedances of the filter networks. We tuned the design parameters with the optimizer tool in AWR Microwave Office to simultaneously meet all these objectives. Finally, we laid out the circuit and performed electromagnetic simulations in AWR Axiem to verify and further refine the circuit design.

It is crucial to note that the output impedances $Z^{(s)}[\omega]$ and $Z^{(p)}[\omega]$ are evaluated assuming 50Ω matching at ports 1 and 2. Experimentally ensuring this matching condition at all frequency bands of interest is essential for the design to function in the physical implementation.

This filter-coupled SNAIL parametric amplifier, henceforth referred to as the F-SPA, was fabricated using a single-step electron beam lithography process on a silicon wafer as described in Appendix A. Fig. 3(b) presents an optical microscope image of the device, with an inset electron microscope image showing the array of 10 SNAILs, fabricated using a Dolan bridge process.

IV. F-SPA CHARACTERIZATION AND COMPARISON WITH A REGULAR SPA

In this section, we report the characterization of the performance of the F-SPA described in the last section. To demonstrate the advantage of the F-SPA, we compare its power efficiency, pump leakage, and noise performance with that of a standard capacitor-coupled SPA (referred to in the following as C-SPA)[8, 15].

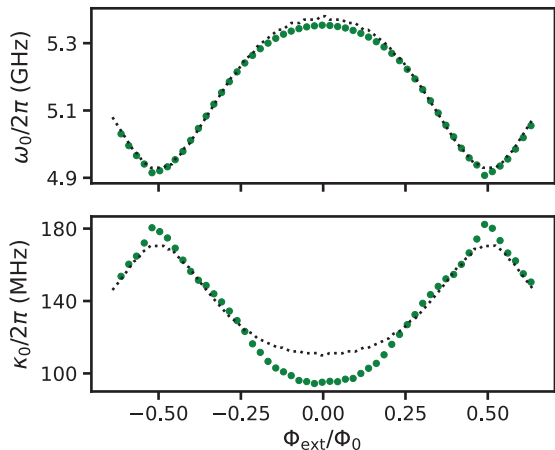


FIG. 4: Resonance frequency ω_0 and linewidth κ_0 of the device as functions of external flux, showing agreement between simulation (dashed lines) and measurement (points).

We first measure the linear reflection from port 1 to extract the resonance frequency and linewidth of the F-SPA mode at different external flux bias Φ_{ext} , as shown in Fig. 4. The measured resonance frequency agrees well with that from the AWR Axitem simulation over the full flux tunable range of the device. The measured linewidth, however, is noticeably lower than that from simulation near zero external flux. This deviation is likely caused by fabrication uncertainty that shifts the pass band of the signal port filter, and impedance mismatch on this port. Due to the low-pass nature of this radial-stub filter, the linewidth of the F-SPA mode is more sensitive to the frequency roll-off of the filter when in the high frequency part of its tunable range.

At each flux bias point, we then apply from port 2 a pump tone at frequency $\omega_p = 2\omega_0$ with the power that generates a small-signal 20 dB phase-preserving gain in reflection. Under this condition, we measure the pump leakage power P_{leak} (at port 1), output signal 1 dB compression power $P_{\text{1dB}}^{\text{out}}$ and the added noise at the frequency 100 kHz below ω_0 .

The same characterization of a C-SPA is performed with identical measurement setup. The C-SPA is implemented by embedding the SNAIL array at the current antinode of a half-wave transmission line resonator, with a large coupling capacitance at port 1 and a small coupling capacitance at port 2. For a fair comparison,

the resonance frequency, linewidth and 3-wave mixing strength of these two devices are designed to be nominally identical. The resonance frequencies of both the F-SPA and the C-SPA are designed to be between 4.5 GHz and 5.5 GHz such that their pump frequencies, between 9.0 GHz and 11.0 GHz, are within the pass band of the microwave components on the output line. Due to fabrication uncertainty, the linewidth of the C-SPA turned out in the range of 60 to 90 MHz, approximately a factor of two smaller than that of the F-SPA. This would result in about 6 dB lower pump power required for the same 20 dB gain.

As shown in Fig. 5(a), the F-SPA requires 20 to 25 dB less pump power than the C-SPA to generate 20 dB gain across the full operating range. The F-SPA shows higher $P_{\text{1dB}}^{\text{out}}$ due to its larger linewidth compared to the C-SPA. Overall, the F-SPA achieves an average power efficiency of $\eta_p = 3 \times 10^{-3}$, which is 30 dB better than the C-SPA and consistent with the 27 dB improvement predicted by our linear circuit simulation.

The pump leakage power, as plotted in Fig. 5(b), is on average -113 dBm for the F-SPA and -77 dBm for the C-SPA. This dramatic 36 dB improved suppression in pump leakage on the F-SPA originates from the combination of the improved pump coupling efficiency and the reflectivity from the signal-port filter.

It is worth pointing out that the pump for a typical 3-wave-mixing JPA could fall outside the band of the circulators between the signal source and the JPA. The out-of-band reverse isolation of the circulators are generally not optimized. It is therefore of practical advantage to suppress pump leakage at the device level instead of relying on external components.

The added noise temperature (with respect to the input signal) of these two amplifiers are shown in Fig. 5(c). The added noise and output power of the amplifiers are calibrated using a shot noise tunnel junction (SNTJ)[31] as explained in Appendix A. Both devices have added noise that are at most twice the quantum limit for phase-preserving amplification[32]. The excess added noise is consistent for both devices, which is most likely due to residual thermal noise from the signal input line. Thermal noise from the pump line, on the other hand, does not contribute to added noise in these measurements as we will discuss in the next section.

V. ROBUSTNESS AGAINST PUMP PORT THERMAL NOISE ON THE F-SPA

The F-SPA requires significantly less pump power to operate compared to the C-SPA, leading to a reduced heat load to the dilution refrigerator from power dissipation on the pump line cryogenic attenuators. In this section, we investigate the effect of thermal noise from the pump line on these two devices. Remarkably, we demonstrate that the F-SPA maintains its near quantum-limited noise performance even when exposed to 4 K

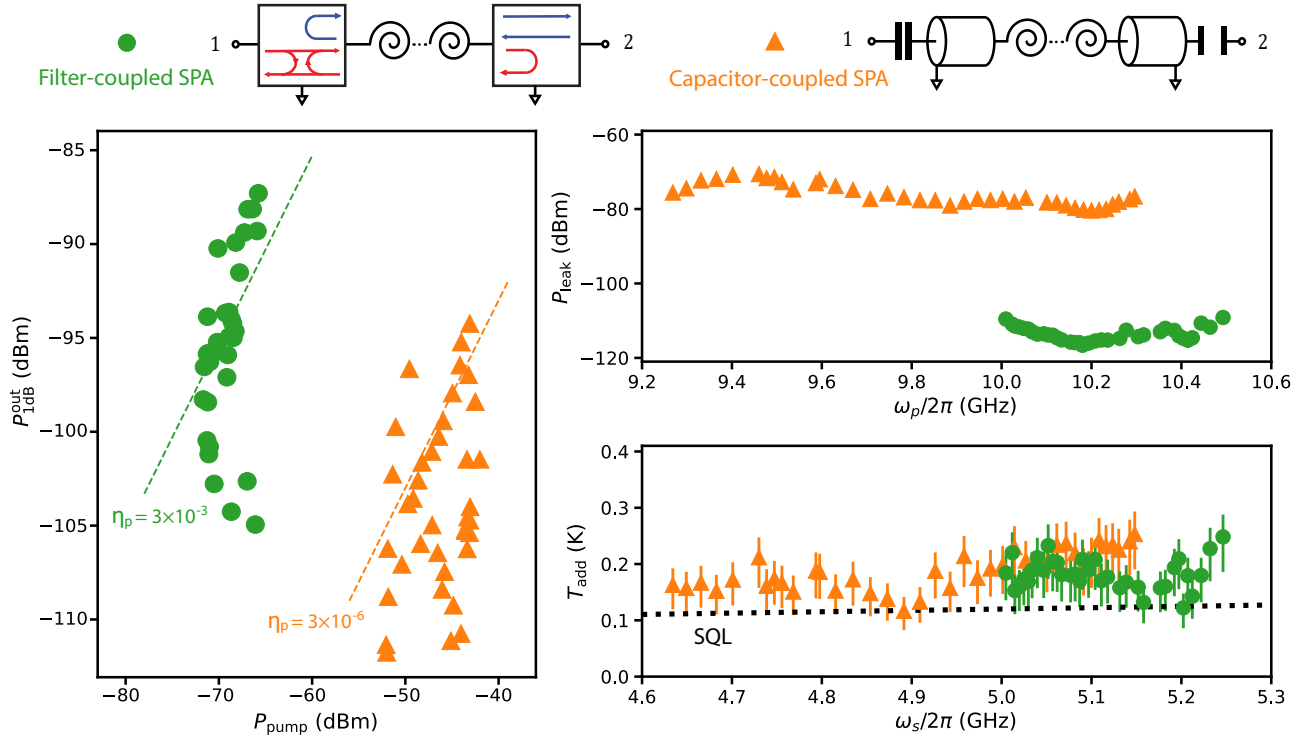


FIG. 5: Characterization of the F-SPA (green dots) and C-SPA (orange triangles) with 20 dB reflection gain over their operating frequency ranges. (a) Output signal power at 1 dB compression points versus pump power at device pump port. Positions of the sloped lines indicates power efficiency η_p . (b) Pump leakage power measured at device signal port. (c) Added noise temperature T_{add} , with a black dashed line indicating the standard quantum limit $\hbar\omega/2k_B$.

noise from the pump port. This characteristic affords an opportunity for further heat load reduction by decreasing the pump line attenuation at the millikelvin stage of the refrigerator.

To achieve quantum-limited noise performance on an amplifier, the signal port input noise temperature $T_N^{\text{in},1}$ must be thermalized to the quantum noise level. The quantum limit of half quanta added noise for a phase-preserving parametric amplifier originates from the input quantum noise at the idler frequency ($\omega_i = \omega_p - \omega_s$). Having another port for pump power delivery, however, introduces additional channels for added noise.

To quantify the effect of pump port input noise on amplifier noise performance, we inject noise along with the coherent pump tone into the pump line and measure the output noise of the amplifier, as illustrated in Fig. 6(a). The injected noise is produced by mixing an artificially generated noise, which has a flat-top power spectrum density from DC to 1 GHz, with a local oscillator near signal and pump frequency, respectively. In this way, we separately investigate the effects of the noise in the signal and idler frequency bands (referred to as signal-band noise, the idler frequency for a degenerate amplifier is usually close to the signal frequency) and the noise in the pump frequency band (referred to as pump-band

noise) respectively. The output noise power spectral density is measured at the frequency ω_s of 20 dB small-signal phase-preserving gain. Both input and output noise power spectral densities are calibrated into noise temperatures $T_N[\omega]$ at the device ports (Appendix A). We perform this experiment on the F-SPA at $\omega_s/2\pi = 5.04$ GHz and the C-SPA at $\omega_s/2\pi = 4.76$ GHz, which corresponds to the operating points with highest $P_{1\text{dB}}$ for the two devices respectively.

Without noise injection, the output noise of both the F-SPA (marked circle) and the C-SPA (marked triangle) are close to the quantum limit, given by $T_N^{\text{out},1}[\omega_s] = G \cdot \hbar\omega_s/k_B$. Upon injecting noise in the signal and idler frequency bands, the output noise temperature increases linearly with the pump-port input noise temperature. As indicated by the yellow curved lines in Fig. 6(b), the F-SPA is characterized by a fitted linear coefficient of 0.30, while the C-SPA exhibits a higher coefficient of 3.6. This coefficient should equal to twice the signal transmission coefficient defined in Eq.8 due to reciprocity of transmission at both the signal and idler frequencies. Compared to the C-SPA, the F-SPA exhibits an order of magnitude better suppression against signal-band noise from the pump line. Notably, the F-SPA maintains near quantum-limited performance even with noise injection up to 4 K,

showing only a minimal increase in added noise amounting to 0.05 quanta. This robust performance indicates that the thermalization requirement for the pump line of F-SPA can be significantly relaxed compared to conventional designs.

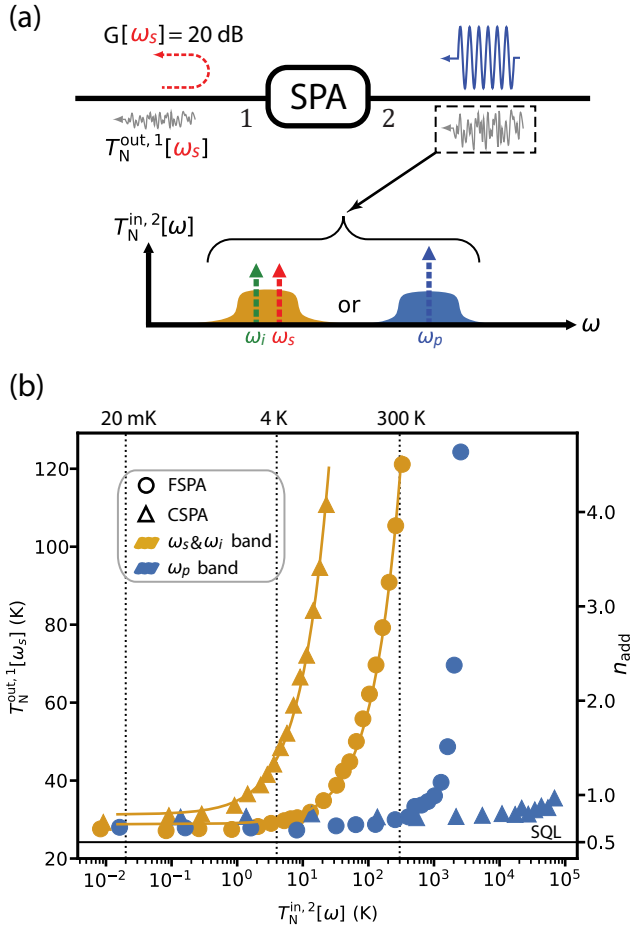


FIG. 6: Pump line noise injection experiment. (a) Experimental setup: output noise temperature from the signal port is measured as a function of the pump port input noise temperature, under the 20 dB gain pumping condition. (b) Data obtained from F-SPA (circles) and C-SPA (triangles) under injected noise in signal and idler frequency bands (yellow) and pump frequency band (blue) respectively. Yellow lines represent linear fits to the data, with fitted slope 3.6 for the C-SPA and 0.30 for the F-SPA. The black horizontal line indicates the standard quantum limit (SQL) of the added noises.

When injecting noise at pump frequency, the output noise temperature of the F-SPA starts to increase drastically (i.e. beyond linear dependence) at a pump-band noise temperature of 10^3 K, as shown in 6(b). In contrast, the output noise temperature of the C-SPA barely starts to increase at 10^5 K of pump-band noise. This 20 dB difference in the threshold pump-band noise temperature is just another manifestation of the improved

pump coupling efficiency on the F-SPA. However, the exact mechanism behind how pump-band noise cause signal-bands output noise to increase requires further investigation.

Improving the pump coupling efficiency indeed increases the susceptibility of F-SPA to noise at the pump frequency. However, this should not degrade its noise performance in standard applications where the pump-band noise temperature typically remains well below 1000 K. On the other hand, the filtering at the pump port of the F-SPA provides improved suppression of signal-band noise, thereby offering an opportunity for substantial heat load reduction. This reduction may be achieved through decreasing or potentially eliminating attenuation at the millikelvin stage of the dilution refrigerator.

VI. CONCLUSION AND DISCUSSION

In this work we have demonstrated a 3 orders of magnitude improvement in both power efficiency and pump leakage suppression on a filter-coupled SNAIL parametric amplifier compared to a regular capacitor-coupled counterpart. This improvement is achieved by implementing 3-stage, on-chip filters on the signal and pump ports of the device. Most previous work incorporating microwave filters into JPA design were targeted at improving the bandwidth and dynamic range[5, 9, 11, 12]. Our work addresses the increasingly important issue of pump power delivery for 3-wave-mixing JPAs. While a recent study [12] discussed the use of an external diplexer to facilitate pump delivery, our work provides the methodology for optimizing the pump coupling at the device design level. The on-chip filtering strategy offers advantages in terms of compactness and eliminates insertion loss from additional external components. Moreover, the network-based description we introduced, particularly the formulation of the resonance condition in terms of Thevenin impedance, provides a systematic framework for designing the embedding circuit for Josephson elements with frequency-dependent coupling to the environment. We believe the strategy of including microwave filters in circuit QED design should benefit many other applications featuring off-resonant parametric drives[33–37].

Moreover, our work shows the benefits of the signal-pump frequency separation of 3-wave mixing amplifiers, which allows for substituting pump line attenuation with filtering, reducing both the cryogenic power dissipation and the overall pump power required from the room-temperature rf generator. In particular, the filter-coupled SPA is robust against thermal noise on the pump port with up to 4 K noise temperature. This demonstration opens up the possibility for eliminating attenuation at the millikelvin stage of the dilution refrigerator, and for introducing a separate port for pumping kinetic-inductance-based parametric amplifiers that can operate at higher temperature[38]. Such optimizations will greatly alleviate the challenge of operating a large array of quantum-

limited amplifiers in a large-scale superconducting quantum processor.

VII. ACKNOWLEDGEMENT

The authors want to thank José Aumentado for providing the shot noise tunnel junction used for noise calibration. We acknowledge Nicholas Frattini and Benjamin Chapman for helpful discussions. W.D. thanks Luigi Frunzio, Robert Schoelkopf, and A. Douglas Stone for their advice on this project. This material is based upon work supported by the U.S. Department of Energy, Office of Science, National Quantum Information Science Research Centers, Co-design Center for Quantum Advantage (C2QA) under contract number DE-SC0012704. S.S. acknowledges support from the Air Force Office of Scientific Research (grant numbers FA9550-20-1-0177, FA9550-22-1-0203) and the Army Research Office (grant numbers W911NF-23-1-0096, W911NF-23-1-0251). Fabrication facilities use was supported by the Yale Institute for Nanoscience and Quantum Engineering (YINQE) and the Yale SEAS Cleanroom. The views and conclusions contained in this document are those of the authors and should not be interpreted as representing the official policies, either expressed or implied, of the US Government. The US Government is authorized to reproduce and distribute reprints for Government purposes notwithstanding any copyright notation herein.

Appendix A: Device fabrication and measurement setup

The fabrication and packaging processes of our device are originally developed and introduced in Ref. [8, 15]. The aluminum strip (bright pattern in Fig. 3(b)) along with an array of $M = 10$ SNAILS embedded inline is fabricated with a single-step e-beam lithography and lift-off process. Each SNAIL consists of three large Josephson junctions with critical current $I_c = 10.1 \mu\text{A}$ in parallel with one small junction with critical current $I_c = 0.8 \mu\text{A}$, all formed by the Dolan bridge process, as shown in the SEM image in Fig. 3(b) inset.

The microstrip ground plane is formed by 2 μm thick layer of silver on the back of a 300 μm thick silicon substrate. The silver back plane of the chip is glued using conducting silver paste to the copper back plane of a printed circuit board (PCB), which is soldered to a gold-plated aluminum box. The signal and pump aluminum transmission line traces on the chip are wire-bonded to the copper transmission line traces on the PCB, which are soldered to edge-mount SMA connectors.

A schematic of the cryogenic microwave measurement system used in this experiment is shown in Figure.7. All measurements were performed with a Keysight PNA-X N5242A network analyzer, with the scattering parameters measured with the SMC (Scaler Mixer/Converter)

measurement class, and the noise temperature measured with the NF (Noise Figure) measurement class.

The FSPA and CSPA were measured with the same wiring setup in two consecutive cooldowns, and in a third cooldown we used a Shot-Noise Tunnel Junction (SNTJ) [39] to calibrate the output chain. When measuring the CSPA device, a lowpass filter was added to the output chain in order to prevent the pump leakage from saturating the room temperature MITEQ amplifier. The two output line setups, with and without the lowpass filter, are calibrated respectively with the SNTJ.

1. Noise calibration

The SNTJ serves as a self-calibrated noise source [31] with which we can calibrate the gain G_{sys} and noise temperature T_{sys} of the output chain, shown in Figure.8. The uncertainty for noise temperature calibration is dominated by the impedance mismatch on the SNTJ and loss in the bias-tee, and we accordingly extract the errorbar as a function of frequency.

We then measured the noise visibility ratio (NVR) of the FSPA and CSPA, defined as the ratio between the noise power spectral density with the JPA on and off ($\text{NVR} = P_N^{\text{on}}/P_N^{\text{off}}$. When measuring P_N^{off} the pump line noise injection is turned off along with the coherent pump). The JPA output noise $T_N^{\text{out},1}$ is extracted from:

$$\text{NVR} = \frac{G_{\text{sys}}(T_{\text{sys}} + T_N^{\text{out},1})}{G_{\text{sys}}(T_{\text{sys}} + T_Q)} \quad (\text{A1})$$

using the T_{sys} calibrated by the SNTJ.

The added noise temperature plotted in Fig. 5 is obtained with the assumption that the signal port input noise is quantum limited: $T_N^{\text{out},1} = G(T_Q + T_{\text{add}})$, which tends to be a pessimistic estimate for the JPA noise performance, since the input thermal noise gets combined with the amplifier added noise.

2. Pump noise injection

In the noise injection experiment presented in Section V, we used a noise generator NOD-5200 to produce a stochastic rf signal with a flat spectrum up to 1 GHz, and used a Marki M8-0420HS mixer to up-convert its frequency. The center frequency of the noise spectrum (set by the LO frequency in the mixing process) is 600 MHz detuned from the signal or pump frequency, to minimize any unwanted effect from the LO leakage tone. A 10 dB attenuator is applied after the mixer to suppress the LO leakage as well.

We measured the noise power spectrum before the combiner, and used the pump line attenuation measured at room temperature to calibrate the input noise temperature $T_N^{\text{in},2}$ at device level.

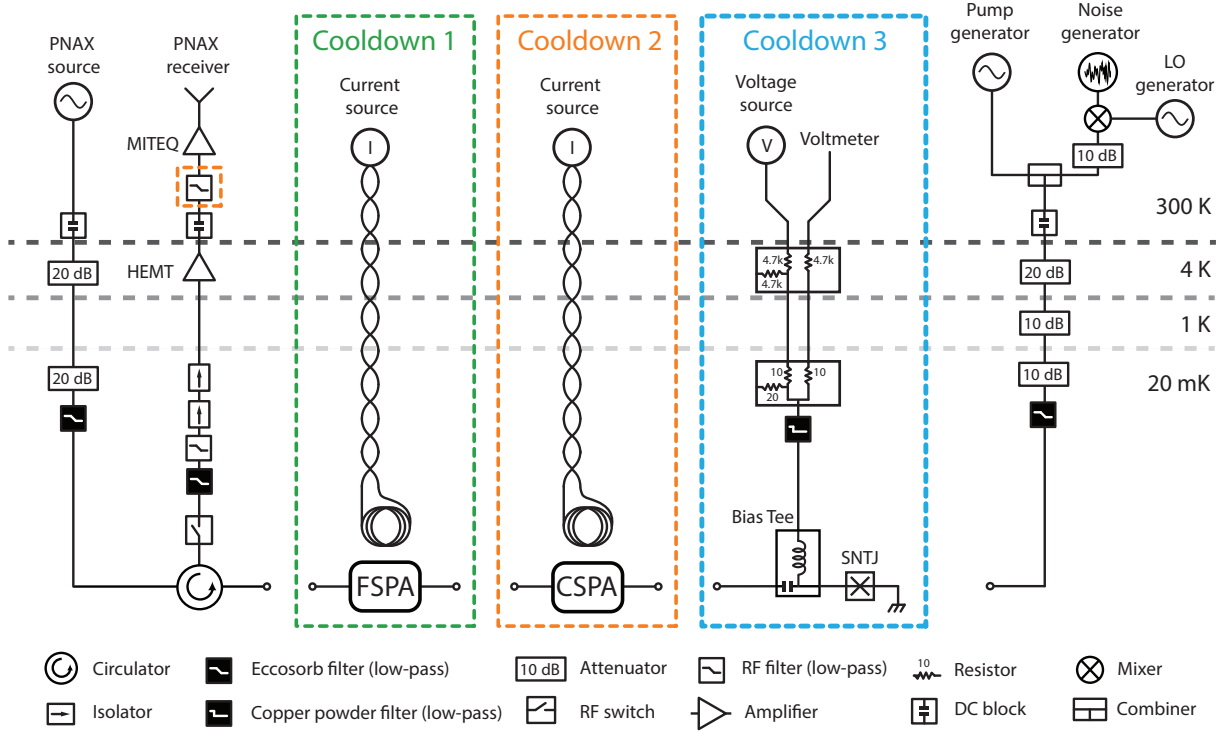


FIG. 7: Schematic of the cryogenic microwave wiring setup in this experiment. Parts of the setup enclosed in dashed boxes were connected in-line in separate cooldowns.

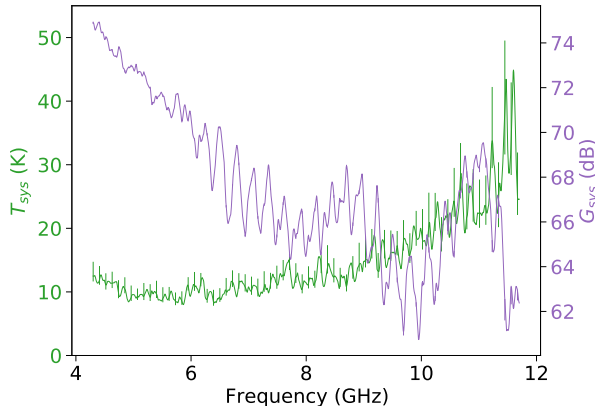


FIG. 8: Output line gain and noise temperature calibrated with a SNTJ.

Appendix B: Scattering parameter and linear network analysis

In this appendix we provide some details on linear network analysis that support the results we reported in Section II and III. In B.1 we derive the relations between wave components defined from the 3-port network modeled by Fig. 2. In B.2 we show the simulation results of

the signal-port filter and pump-port filter as in Fig. 3, and discuss how they are related to the 3-port network parameters using the signal flow graph analysis.

1. Scattering analysis for the 3-port network

The scattering parameters for a network is defined as $S_{ij} = \frac{V_{in,i}^{out}}{V_{in,j}^{in}} \Big|_{V_{in,k \neq j} = 0}$, the transfer function from port j input to port i output with all ports terminated by Z_0 .

For the 3-port network shown in Fig. 10(a), port 3 is terminated by the Josephson dipole which we treat as a linear load. Therefore, the Josephson dipole reflects the port 3 outgoing wave back into the network: $V_{in,3} = \Gamma_3 V_{out,3}$. So the total voltage across the two terminals of port 3 (i.e. across the Josephson dipole) is:

$$V^J = V_{in,3} + V_{out,3} = (1 + \Gamma_3) V_{out,3}. \quad (\text{B1})$$

Using the network scattering parameters, $V_{out,3}$ can be evaluated as

$$\begin{aligned} V_{out,3} &= S_{33} V_{in,3} + S_{31} V_{in,1} + S_{32} V_{in,2} \\ &= \frac{S_{31}}{1 - \Gamma_3 S_{33}} V_{in,1} + \frac{S_{32}}{1 - \Gamma_3 S_{33}} V_{in,2} \end{aligned} \quad (\text{B2})$$

from which we can obtain the relation in equation (4) considering the pump applied only from port 2 (i.e. $V_p^{in,1} = 0$).

The signal, on the other hand, is applied only from port 1 (i.e. $V_s^{\text{in},2} = 0$). Similar expression for $V^{\text{out},1}$ and $V^{\text{out},2}$ can be evaluated accordingly, that gives rise to equation (6) and (8) respectively.

2. Signal flow graph analysis for concatenating two-port networks

In Section II we formulated the goals for circuit synthesis in terms of scattering parameters on a 3-port network. Since it is somewhat tricky to design the 3-port distributed-element circuit directly, we chose to decompose the circuit into separately designed signal-port and pump-port filter networks. The 2-port scattering matrix of the signal-port network is represented as

$$S^{(s)} = \begin{pmatrix} r^{(s)} & t^{(s)} \\ t^{(s)} & r^{(s)} \end{pmatrix} \quad (\text{B3})$$

and similarly for the pump-port network, denoted as $S^{(p)}$, where t , r and r' are labeled in the signal flow diagram in Fig. 10(c).

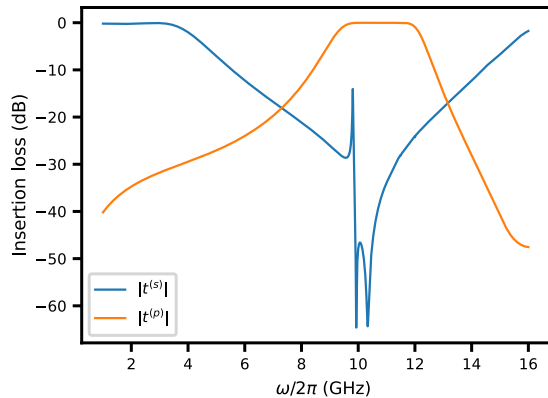


FIG. 9: Simulated insertion loss of the signal-port filter and the pump-port filter respectively.

As discussed in Section III, the pump-port network is designed to pass the pump (around 10 GHz) and reject the signal (around 5 GHz), which is realized with a band-pass filter. The signal-port network is designed to create a stopband around pump frequency while placing the signal frequency within its transition band, for controlling the damping rate κ_0 of the resonant mode. The insertion loss of the two filter networks from AWR Axiem simulation are plotted in Fig.(9).

The standard filter designs typically aim to optimize the insertion loss $|t|$ and return loss $|r|$, assuming both ports are Z_0 matched. However, in our device the networks combine in the following manner: the Josephson dipole connects a pair of terminals, and the other pair of terminals are galvanically connected via the microstrip

ground. Signal-flow graph analysis[29] can be applied to Fig. 10(c) to construct the effective 3-port scattering matrix for the concatenated circuit.

$$S_{31} = \frac{2(1 - r^{(p)})t^{(s)}}{3 - (r^{(s)} + r^{(p)}) - r^{(s)}r^{(p)}} \quad (\text{B4})$$

$$S_{32} = \frac{2(1 - r^{(s)})t^{(p)}}{3 - (r^{(s)} + r^{(p)}) - r^{(s)}r^{(p)}} \quad (\text{B5})$$

$$S_{21} = \frac{2t^{(s)}t^{(p)}}{3 - (r^{(s)} + r^{(p)}) - r^{(s)}r^{(p)}} \quad (\text{B6})$$

$$S_{33} = \frac{1 + (r^{(s)} + r^{(p)}) - 3r^{(s)}r^{(p)}}{3 - (r^{(s)} + r^{(p)}) - r^{(s)}r^{(p)}} \quad (\text{B7})$$

In addition, the signal-flow graph analysis also gives us the linear response relations of interest between the voltage across the Josephson dipole and the input voltage, e.g. from the signal port,

$$V^J = \frac{\frac{2}{3}t^{(s)}(1 - r^{(p)})}{1 - \frac{1}{3}r^{(s)}r^{(p)} - \frac{1}{3}(r^{(s)} + r^{(p)})} V^{\text{in},1}. \quad (\text{B8})$$

The most important consideration in our design process is the precise control of the resonant mode frequency and damping rate, which we will explain in detail in the next appendix.

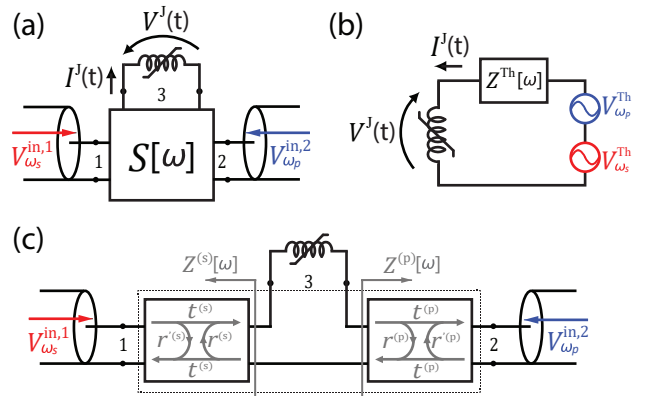


FIG. 10: Three equivalent descriptions of a Josephson-dipole-based parametric amplifier, modeling the linear circuit by (a) a 3-port network (b) a Thevenin equivalent circuit (c) the combination of 2-port networks.

Appendix C: Resonance condition from Thevenin circuit method

In this appendix, we formulate the resonance condition for a general circuit containing a lumped Josephson dipole, such as the example shown in Fig. 10(a).

Our method can efficiently extract the resonance frequency, damping rate, and *Josephson participation ratio* [40] of a classical mode, whose Kerr nonlinearity is much smaller than its damping rate. We expect our method to provide some insights into designing Josephson-element-based parametric amplifiers and couplers with complicated embedding circuits.

According to the AC Thevenin theorem, the two-terminal linear bilateral circuit external to the Josephson dipole can be replaced by a Thevenin equivalent circuit consisting of a single impedance $Z^{\text{Th}}[\omega]$ in series with a single voltage source $V^{\text{Th}}(t)$, as depicted in Fig. 10(b). The external voltage source has only two harmonic components (i.e. signal and pump) and thus $V^{\text{Th}}(t) = \text{Re}(V_{\omega_s}^{\text{Th}} e^{j\omega_s t} + V_{\omega_p}^{\text{Th}} e^{j\omega_p t})$.

For obtaining the linear eigenmode of the system, we replace the nonlinear Josephson dipole by its inductance L_J , with a linear response: $V^J = L_J \frac{dI^J}{dt}$. To find the ‘undriven’ modes of motion allowed by a homogeneous linear system, a Laplace transform (represented by \mathcal{L}) can be applied to the equation of motion [41]:

$$sL_J \mathcal{L}\{I^J(t)\} + Z^{\text{Th}}(s) \mathcal{L}\{I^J(t)\} = 0 \quad (\text{C1})$$

This gives rise to the *resonance condition*, shown as equation (5) in Section II. The general solution to the system can always be decomposed into a linear combination of eigenmode excitations:

$$I^J(t) = \sum_a I_a e^{-\frac{\kappa_a}{2}t + j\omega_a t} \quad (\text{C2})$$

using the discrete set of solutions $\{s_a = j\omega_a - \frac{\kappa_a}{2}\}$ to equation (5).

Next, we bridge between Laplace domain functions and Fourier domain functions, in order to formulate the resonance condition in terms of Fourier domain response function $Z^{\text{Th}}[\omega]$ which is easier to obtain from linear circuit simulation. We use the notation that the Fourier domain function $f[\omega]$ equals the Laplace domain function $f(s)$ taken on the imaginary axis $s = j\omega$. Note that we have the following identity with respect to their derivatives:

$$\begin{aligned} f'[\omega] &:= \frac{f[\omega + d\omega] - f[\omega]}{d\omega} \\ &= \frac{f(j\omega + jd\omega) - f(j\omega)}{d\omega} \\ &=: j f'(j\omega) \end{aligned} \quad (\text{C3})$$

Assuming $\kappa_a \ll \omega_a$, the following approximation from Taylor expansion:

$$f(j\omega_a - \frac{\kappa_a}{2}) \approx f(j\omega_a) - \frac{\kappa_a}{2} f'(j\omega_a)$$

holds for any analytic function $f(s)$. Therefore, we can write:

$$Z^{\text{Th}}(j\omega_a - \frac{\kappa_a}{2}) \approx Z^{\text{Th}}[\omega_a] + j \frac{\kappa_a}{2} Z^{\text{Th}'}[\omega_a] \quad (\text{C4})$$

Plugging in the resonance condition Eq. 5 in the main text, i.e. $Z^{\text{Th}}(j\omega_a - \frac{\kappa_a}{2}) = -j\omega_a L_J + \frac{\kappa_a}{2} L_J$:

$$\text{Im}Z^{\text{Th}}[\omega_a] = -\left(\omega_a L_J + \frac{\kappa_a}{2} \text{Re}Z^{\text{Th}'}[\omega_a]\right) \quad (\text{C5a})$$

$$\text{Re}Z^{\text{Th}}[\omega_a] = \frac{\kappa_a}{2} \left(L_J + \text{Im}Z^{\text{Th}'}[\omega_a]\right) \quad (\text{C5b})$$

These are the requirements on $Z^{\text{Th}}[\omega]$ (both real and imaginary part) that we synthesize for a resonance mode with frequency $\omega_a/2\pi$ and linewidth $\kappa_a/2\pi$.

The Thevenin impedance for our design can either be expressed in terms of the 3-port network scattering parameter:

$$Z^{\text{Th}}[\omega] = Z_0 \frac{1 + S_{33}[\omega]}{1 - S_{33}[\omega]} \quad (\text{C6})$$

or be separated into two parts: $Z^{\text{Th}}[\omega] = Z^{(s)}[\omega] + Z^{(p)}[\omega]$ where

$$Z^{(s)}[\omega] = Z_0 \frac{1 + r^{(s)}[\omega]}{1 - r^{(s)}[\omega]} \quad (\text{C7a})$$

$$Z^{(p)}[\omega] = Z_0 \frac{1 + r^{(p)}[\omega]}{1 - r^{(p)}[\omega]} \quad (\text{C7b})$$

are the output impedance towards signal and pump port respectively, as indicated in Fig. 10(c).

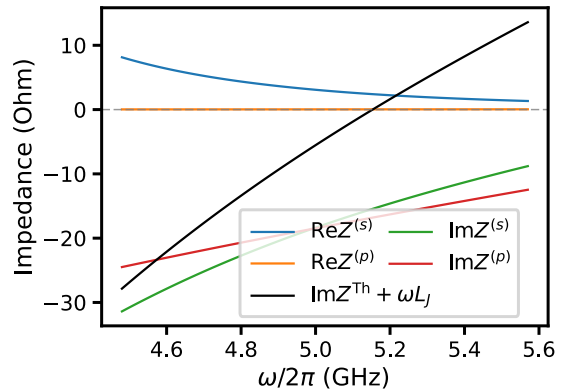


FIG. 11: Simulated output impedance towards signal port $Z^{(s)}$ and output impedance towards pump port $Z^{(p)}$. The resonance frequency is determined by the point where the black curve (an example with $L_J(\Phi_{\text{ext}})$ evaluated at $\Phi_{\text{ext}} = 0.3\Phi_0$) crosses 0. The slope at this point is related to the Josephson participation of the mode. Real part of $Z^{(s)}$ evaluated at the resonance frequency determines the linewidth of the mode.

In Fig. 11, we show the $Z^{(s)}$ and $Z^{(p)}$ simulated (using AWR Axiem) around the desired resonance frequency. We also plot the imaginary part of $Z^{(s)}[\omega] + Z^{(p)}[\omega] + j\omega L_J(\Phi_{\text{ext}})$ evaluated at $\Phi_{\text{ext}} = 0.3\Phi_0$ as the black curve. As the second term on the right hand side of Eq.(C5a)

is negligible in our case, the resonance frequency ω_a is essentially the point where the black curve crosses 0. We then evaluate κ_a from Eq.(C5b), using $\text{Re}Z^{\text{Th}}$ and $\text{Im}Z^{\text{Th}'}$ taken at ω_a . Since the real part of $Z^{(p)}$ is almost 0 around resonance frequency (as the pump-port filter rejects the on-resonance signal), the damping rate of the mode originates entirely from the dissipation at signal port.

In Fig. 3(c) from the main text we have shown the resonance frequency and linewidth extracted using the method above, with varying $L_J(\Phi_{\text{ext}})$ for the SNAIL array[28]. They agree with the experimental results fairly well.

Lastly, we can also extract the *Josephson inductive participation ratio* of each mode a from the Thevenin circuit method. Following the same ideas as blackbox circuit quantization[42], the Josephson dipole can be expressed as a linear inductor L_J in parallel with a purely nonlinear element. Under the assumption of weak dissipation (i.e. $\kappa_a \ll \omega_a$) for all eigenmodes of interest, the full linear circuit consisting of L_J in parallel with the Thevenin impedance can be decomposed into a set of poles in the form of parallel RLCs, i.e. an approximate Foster-equivalent admittance.

$$\frac{1}{sL_J} + \frac{1}{Z^{\text{Th}}(s)} = \sum_a \left(sC_a + \frac{1}{sL_a} + \frac{1}{R_a} \right) \quad (\text{C8})$$

Combining this with the resonance condition Eq. 5, we can arrive at the following result:

$$p_a^J := \frac{L_a}{L_J} \approx \frac{2}{1 + \frac{\text{Im}Z^{\text{Th}'[\omega_a]}}{L_J}} \quad (\text{C9})$$

which by definition is the inductive participation ratio (twice the energy participation ratio as defined in [40]) of the Josephson dipole in mode a .

An observation is made that p_a^J enters equation (C5b) such that $\text{Re}Z^{\text{Th}}[\omega_a]/L_J = \kappa_a/p_a^J$. It can be understood as a scaling factor between the damping rate at the Josephson dipole and that for the resonance mode.

Appendix D: Modeling the pumped Josephson dipole

In this appendix, we introduce a circuit model describing a current-pumped parametric process in a single lumped Josephson dipole, in analogy with previous work on flux-pumped parametric processes [26]. This description applies to the synthesis of parametric amplifiers and converters, as well as of the current-pumped ancilla for gaussian operations on bosonic modes [36, 43, 44].

Similar to the Taylor expansion of the Josephson relation $I = \frac{\phi_0}{L_J} \sin \varphi$ for a single Josephson junction, the electric current $I^J(t)$ is linked to the superconducting phase $\varphi^J(t) = \Phi^J(t)/\phi_0$ across an arbitrary

Josephson dipoles (such as the SNAIL[28], rf SQUID or Gradiometric-SNAIL[45]) by the following relation:

$$I^J = \frac{\phi_0}{L_J} \left(\varphi^J + \frac{c_3}{2} \varphi^{J2} + \dots \right) \quad (\text{D1})$$

Here, we keep only the 3rd order of nonlinearity and study the parametric squeezing processes arising from this term.

Consider a pump at $\omega_p = \omega_s + \omega_i$ applied to activate squeezing between two temporal modes centered at ω_s and ω_i respectively (which holds for phase-preserving amplification). We decompose $I^J(t)$ and $\varphi^J(t)$ in equation (D1) using the phasor representation:

$$\begin{aligned} I^J(t) &= \text{Re} \left(I_p^J e^{j\omega_p t} + I_s^J e^{j\omega_s t} + I_i^J e^{j\omega_i t} \right) \\ \varphi^J(t) &= \text{Re} \left(\varphi_p^J e^{j\omega_p t} + \varphi_s^J e^{j\omega_s t} + \varphi_i^J e^{j\omega_i t} \right) \end{aligned} \quad (\text{D2})$$

Plugging it into equation (D1), the following relations are obtained from harmonic balance:

$$\begin{aligned} I_s^J &= \frac{\phi_0}{L_J} \left(c_2 \varphi_s^J + \frac{c_3}{2} \varphi_p^J \varphi_i^{J*} \right) \\ I_i^{J*} &= \frac{\phi_0}{L_J} \left(c_2 \varphi_i^{J*} + \frac{c_3}{2} \varphi_p^{J*} \varphi_s^J \right) \end{aligned} \quad (\text{D3})$$

The stiff pump approximation assumes that the existence of probes at other frequencies does not affect the steady state $V_{\omega_p}^J$ evaluated from linear circuit analysis. Under such an approximation, the harmonic component $\varphi_p^J = \frac{V_p^J}{j\omega_p \phi_0}$ can be treated as a *parameter* (instead of a *variable*). The harmonic balance equation (D3) between ω_s and ω_i harmonic components is thus linearizable, which can be written as a cross-admittance matrix:

$$\begin{pmatrix} I_s^J \\ I_i^{J*} \end{pmatrix} = \frac{1}{jL_J} \begin{pmatrix} \frac{1}{\omega_s} & \frac{c_3}{2} \frac{\varphi_p^J}{\omega_s} \\ \frac{c_3}{2} \frac{\varphi_p^{J*}}{\omega_s} & \frac{1}{\omega_i} \end{pmatrix} \begin{pmatrix} V_s^J \\ V_i^{J*} \end{pmatrix} \quad (\text{D4})$$

where the off-diagonal term arises from the pump and takes the steady state φ_p^J as a parameter.

In the case of phase-preserving parametric amplification, there is an external signal probe at ω_s only, while no probe is applied at the idler frequency ω_i , as indicated in Fig. (10). Therefore, the ω_i harmonic component at the Josephson dipole has to satisfy a constraint posed by the passive response of the linear coupling circuit, which can be formulated as:

$$V_i^J + Z^{\text{Th}}[\omega_i] I_i^J = 0 \quad (\text{D5})$$

Solving equation (D4) given this constraint, we arrive at a self-consistent same-frequency response to the signal at the pumped Josephson dipole:

$$\left. \frac{I_s^J}{V_s^J} \right|_{(\text{D5})} = \frac{1}{j\omega_s L_J} + \frac{1}{jL_J \omega_s} \frac{\left| \frac{c_3}{2} \varphi_p^J \right|^2}{\frac{jL_J \omega_i}{Z^{\text{Th}*}[\omega_i]} - 1} \quad (\text{D6})$$

where the second term is labeled $Y^{\text{nl}}(V_p^{\text{J}})$ in the main text, an effective admittance that arises upon pumping as illustrated in Figure 2(c).

Lastly, as we commented in Section II, we need a negative real part from $Y^{\text{nl}}(V_p^{\text{J}})$ in order for the device to serve as an amplifier. That is achieved if the idler (ω_i) is on-resonance with a standing mode, i.e. when $Z^{\text{Th}}[\omega_i]$ satisfies equations (C5) as explained in the previous appendix. Using the definition in equation (C9), the condition for the idler being on-resonance can be rewritten as

$$Z^{\text{Th}}[\omega_i] \approx -j\omega_i L_J \left(1 + j \frac{1}{p_i^{\text{J}} Q_i} \right) \quad (\text{D7})$$

where Q_i is quality factor of the standing mode that the idler tone resides in, and p_i^{J} is Josephson participation of this mode.

As a result,

$$\begin{aligned} Y^{\text{nl}}(V_p^{\text{J}}) &= \frac{1}{j\omega_s L_J} \frac{\left| \frac{c_3}{2} \varphi_p^{\text{J}} \right|^2}{1 - j \frac{1}{p_i^{\text{J}} Q_i} - 1} \\ &\approx -\frac{p_i^{\text{J}} Q_i}{\omega_s L_J} \left| \frac{c_3}{2} \varphi_p^{\text{J}} \right|^2 \end{aligned} \quad (\text{D8})$$

which presents a *negative conductance* viewed at the signal frequency. The last approximation holds under the assumption $p_i^{\text{J}} Q_i \gg 1$, which is a well acknowledged claim that the pQ -product need to be greater than 1 for the amplifier to operate.

As an example, our device is a degenerate amplifier where the idler tone and the signal tone populates the same resonance mode. Under the flux point $\Phi_{\text{ext}} = 0.3\Phi_0$ (the black curve in Fig. 11), the mode has a resonance frequency $\omega_a/2\pi = 5.15$ GHz and linewidth $\kappa_a/2\pi = 137$ MHz, with Josephson participation ratio $p_a^{\text{J}} = 0.36\%$. This corresponds to $p_a^{\text{J}} Q_a = 13.5$.

-
- [1] A. Roy and M. Devoret, Phys. Rev. B **98**, 045405 (2018).
- [2] E. Jeffrey, D. Sank, J. Y. Mutus, T. C. White, J. Kelly, R. Barends, Y. Chen, Z. Chen, B. Chiaro, A. Dunsworth, A. Megrant, P. J. J. O'Malley, C. Neill, P. Roushan, A. Vainsencher, J. Wenner, A. N. Cleland, and J. M. Martinis, Phys. Rev. Lett. **112**, 190504 (2014).
- [3] A. Bienfait, J. J. Pla, Y. Kubo, M. Stern, X. Zhou, C. C. Lo, C. D. Weis, T. Schenkel, M. L. Thewalt, D. Vion, D. Esteve, B. Julsgaard, K. Mølmer, J. J. Morton, and P. Bertet, Nature Nanotechnology (2016), 10.1038/nnano.2015.282.
- [4] B. M. Brubaker, L. Zhong, Y. V. Gurevich, S. B. Cahn, S. K. Lamoreaux, M. Simanovskaia, J. R. Root, S. M. Lewis, S. Al Kenany, K. M. Backes, I. Urdinaran, N. M. Rapis, T. M. Shokair, K. A. van Bibber, D. A. Palken, M. Malnou, W. F. Kindel, M. A. Anil, K. W. Lehnert, and G. Carosi, Phys. Rev. Lett. **118**, 061302 (2017).
- [5] T. Roy, S. Kundu, M. Chand, A. M. Vadiraj, A. Ranadive, N. Nehra, M. P. Patankar, J. Aumentado, A. A. Clerk, and R. Vijay, Applied Physics Letters **107**, 262601 (2015).
- [6] C. Eichler and A. Wallraff, EPJ Quantum Technology **1**, 1 (2014).
- [7] G. Liu, T.-C. Chien, X. Cao, O. Lanes, E. Alpern, D. Pekker, and M. Hatridge, Applied Physics Letters **111**, 202603 (2017).
- [8] N. E. Frattini, V. V. Sivak, A. Lingenfelter, S. Shankar, and M. H. Devoret, Physical Review Applied **10**, 54020 (2018).
- [9] O. Naaman, D. G. Ferguson, A. Marakov, M. Khalil, W. F. Koehl, and R. J. Epstein, in *2019 IEEE MTT-S International Microwave Symposium (IMS)* (2019) pp. 259–262.
- [10] L. Planat, R. Dassonneville, J. P. Martínez, F. Foroughi, O. Buisson, W. Hasch-Guichard, C. Naud, R. Vijay, K. Murch, and N. Roch, Phys. Rev. Appl. **11**, 034014 (2019).
- [11] R. Kaufman, T. White, M. I. Dykman, A. Iorio, G. Sterling, S. Hong, A. Opremcak, A. Bengtsson, L. Faoro, J. C. Bardin, T. Burger, R. Gasca, and O. Naaman, Phys. Rev. Appl. **20**, 054058 (2023).
- [12] R. Kaufman, C. Liu, K. Cicak, B. Mesits, M. Xia, C. Zhou, M. Nowicki, J. Aumentado, D. Pekker, and M. Hatridge, “Simple, High Saturation Power, Quantum-limited, RF SQUID Array-based Josephson Parametric Amplifiers,” (2024), arXiv:2402.19435.
- [13] S. Kundu, N. Gheeraert, S. Hazra, T. Roy, K. V. Salunkhe, M. P. Patankar, and R. Vijay, Applied Physics Letters **114**, 172601 (2019).
- [14] T. C. White, A. Opremcak, G. Sterling, A. Korotkov, D. Sank, R. Acharya, M. Ansmann, F. Arute, K. Arya, J. C. Bardin, A. Bengtsson, A. Bourassa, J. Bouvaird, L. Brill, B. B. Buckley, D. A. Buell, T. Burger, B. Burkett, N. Bushnell, Z. Chen, B. Chiaro, J. Cogan, R. Collins, A. L. Crook, B. Curtin, S. Demura, A. Dunsworth, C. Erickson, R. Fatemi, L. Flores-Burgos, E. Forati, B. Foxen, W. Giang, M. Giustina, A. G. Dau, M. C. Hamilton, S. D. Harrington, J. Hilton, M. Hoffmann, S. Hong, T. Huang, A. Huff, J. Iveland, E. Jeffrey, M. Kieferová, S. Kim, P. V. Klimov, F. Kostritsa, J. M. Kreikebaum, D. Landhuis, P. Laptev, L. Laws, K. Lee, B. J. Lester, A. Lill, W. Liu, A. Locharla, E. Lucero, T. McCourt, M. McEwen, X. Mi, K. C. Miao, S. Montazeri, A. Morvan, M. Neeley, C. Neill, A. Nersisyan, J. H. Ng, A. Nguyen, M. Nguyen, R. Potter, C. Quintana, P. Roushan, K. Sankaragomathi, K. J. Satzinger, C. Schuster, M. J. Shearn, A. Shorter, V. Shvarts, J. Skrzny, W. C. Smith, M. Szalay, A. Torres, B. Woo, Z. J. Yao, P. Yeh, J. Yoo, G. Young, N. Zhu, N. Zobrist, Y. Chen, A. Megrant, J. Kelly, and O. Naaman, Applied Physics Letters **122**, 014001 (2023).
- [15] V. Sivak, N. Frattini, V. Joshi, A. Lingenfelter, S. Shankar, and M. Devoret, Phys. Rev. Appl. **11**, 054060 (2019).

- [16] C. Liu, T.-C. Chien, M. Hatridge, and D. Pekker, *Phys. Rev. A* **101**, 042323 (2020).
- [17] V. V. Sivak, S. Shankar, G. Liu, J. Aumentado, and M. H. Devoret, *Phys. Rev. Appl.* **13**, 024014 (2020).
- [18] A. Kamal, A. Marblestone, and M. Devoret, *Phys. Rev. B* **79**, 184301 (2009).
- [19] M. Simoen, C. W. S. Chang, P. Krantz, J. Bylander, W. Wustmann, V. Shumeiko, P. Delsing, and C. M. Wilson, *Journal of Applied Physics* **118**, 154501 (2015).
- [20] X. Zhou, V. Schmitt, P. Bertet, D. Vion, W. Wustmann, V. Shumeiko, and D. Esteve, *Physical Review B* **89**, 214517 (2014).
- [21] T. Elo, T. S. Abhilash, M. R. Perelshtein, I. Lilja, E. V. Korostylev, and P. J. Hakonen, *Applied Physics Letters* **114**, 152601 (2019).
- [22] J. Y. Mutus, T. C. White, E. Jeffrey, D. Sank, R. Barends, J. Bochmann, Y. Chen, Z. Chen, B. Chiaro, A. Dunsworth, J. Kelly, A. Megrant, C. Neill, P. J. O'Malley, P. Roushan, A. Vainsencher, J. Wenner, I. Siddiqi, R. Vijay, A. N. Cleland, and J. M. Martinis, *Applied Physics Letters* (2013).
- [23] N. M. Hougland, Z. Li, R. Kaufman, B. Mesits, R. S. K. Mong, M. Hatridge, and D. Pekker, "Pump-efficient Josephson parametric amplifiers with high saturation power," (2024), arXiv:2402.12586.
- [24] F. Schackert, A. Roy, M. Hatridge, M. H. Devoret, and A. D. Stone, *Phys. Rev. Lett.* **111**, 073903 (2013).
- [25] K. M. Sundqvist, S. Kintaş, M. Simoen, P. Krantz, M. Sandberg, C. M. Wilson, and P. Delsing, *Applied Physics Letters* **103**, 102603 (2013).
- [26] K. M. Sundqvist and P. Delsing, *EPJ Quantum Technology* **1**, 6 (2014).
- [27] O. Naaman and J. Aumentado, *PRX Quantum* **3**, 020201 (2022).
- [28] N. E. Frattini, U. Vool, S. Shankar, A. Narla, K. M. Sliwa, and M. H. Devoret, *Applied Physics Letters* **110**, 222603 (2017).
- [29] D. M. Pozar, *Microwave engineering; 3rd ed.* (Wiley, Hoboken, NJ, 2005).
- [30] G. Matthaei, E. M. T. Jones, and L. Young, *Microwave Filters, Impedance-Matching Networks, and Coupling Structures* (Artech House, Norwood, Mass, 1980).
- [31] M. Malnou, T. F. Q. Larson, J. D. Teufel, F. Lecocq, and J. Aumentado, *Review of Scientific Instruments* **95**, 034703 (2024).
- [32] C. M. Caves, *Phys. Rev. D* **26**, 1817 (1982).
- [33] A. Grimm, N. E. Frattini, S. Puri, S. O. Mundhada, S. Touzard, M. Mirrahimi, S. M. Girvin, S. Shankar, and M. H. Devoret, *Nature* **584**, 205 (2020).
- [34] P. Campagne-Ibarcq, A. Eickbusch, S. Touzard, E. Zalys-Geller, N. E. Frattini, V. V. Sivak, P. Reinhold, S. Puri, S. Shankar, R. J. Schoelkopf, L. Frunzio, M. Mirrahimi, and M. H. Devoret, *Nature* **584**, 368 (2020).
- [35] C. Zhou, P. Lu, M. Praquin, T.-C. Chien, R. Kaufman, X. Cao, M. Xia, R. S. K. Mong, W. Pfaff, D. Pekker, and M. Hatridge, *npj Quantum Information* **9**, 1 (2023).
- [36] B. J. Chapman, S. J. De Graaf, S. H. Xue, Y. Zhang, J. Teoh, J. C. Curtis, T. Tsunoda, A. Eickbusch, A. P. Read, A. Koottandavida, S. O. Mundhada, L. Frunzio, M. Devoret, S. Girvin, and R. Schoelkopf, *PRX Quantum* **4**, 020355 (2023).
- [37] M. Xia, C. Zhou, C. Liu, P. Patel, X. Cao, P. Lu, B. Mesits, M. Mucci, D. Gorski, D. Pekker, and M. Hatridge, "Fast superconducting qubit control with subharmonic drives," (2023), arXiv:2306.10162.
- [38] M. Xu, Y. Wu, W. Dai, and H. X. Tang, *Applied Physics Letters* **125** (2024).
- [39] L. Spietz, K. W. Lehnert, I. Siddiqi, and R. J. Schoelkopf, *Science* **300**, 1929 (2003).
- [40] Z. K. Mineev, Z. Leghtas, S. O. Mundhada, L. Christakis, I. M. Pop, and M. H. Devoret, *npj Quantum Information* **7**, 1 (2021).
- [41] A. Oppenheim, A. Willsky, and S. Nawab, *Signals & Systems* (Prentice-Hall Inc., 2010).
- [42] S. E. Nigg, H. Paik, B. Vlastakis, G. Kirchmair, S. Shankar, L. Frunzio, M. H. Devoret, R. J. Schoelkopf, and S. M. Girvin, *Phys. Rev. Lett.* **108**, 240502 (2012).
- [43] Y. Y. Gao, B. J. Lester, K. S. Chou, L. Frunzio, M. H. Devoret, L. Jiang, S. M. Girvin, and R. J. Schoelkopf, *Nature* **566**, 509 (2019).
- [44] A. Z. Ding, B. L. Brock, A. Eickbusch, A. Koottandavida, N. E. Frattini, R. G. Cortinas, V. R. Joshi, S. J. d. Graaf, B. J. Chapman, S. Ganjam, L. Frunzio, R. J. Schoelkopf, and M. H. Devoret, "Quantum Control of an Oscillator with a Kerr-cat Qubit," (2024), arXiv:2407.10940.
- [45] A. Miano, G. Liu, V. V. Sivak, N. E. Frattini, V. R. Joshi, W. Dai, L. Frunzio, and M. H. Devoret, *Applied Physics Letters* **120**, 184002 (2022).